Aust. J. Phys., 1990, **43**, 543–64

(e, 2e) Studies of Atoms —Some Recent Developments*

Erich Weigold

Electronic Structure of Materials Centre, Flinders University of South Australia, Bedford Park, S.A. 5042, Australia.

Abstract

Some recent work on (e, 2e) collisions in atoms is reported. The first (e, 2e) results on an excited target and also on an oriented target are discussed. Sodium atoms are pumped to the $m_l = +1$ state of the excited 3p state by σ^+ light from a laser. The (e, 2e) measurements are then performed on this excited state. The results are in excellent agreement with the momentum density profile given by the 3p($m_l = 1$) Hartree-Fock wavefunction. High resolution electron momentum spectroscopy measurements are reported for argon. The first momentum profiles for excited Ar ion states belonging to the $^2P^o$ and $^2D^e$ manifolds are obtained. The latter are entirely due to initial state correlations. Comparison is made with several many-body calculations. The importance of core quadrupole (^1D) excitations is demonstrated. Although the $^2S^e$ manifold is dominated by final state correlations, the momentum profile to the 4s ^2S ion state in the $^2S^e$ manifold also shows the influence of initial state correlation effects. The third series of measurements examines correlations in the autoionising region of helium, encompassing the $(2s^2)^1S$, $(2s2p)^3P$, $(2p^2)^1D$ and $(2s2p)^1P$ resonances, at 100, 200 and 400 eV incident electron energies. Measurements, with an energy resolution of 150 meV, were taken at a number of scattered electron angles over an extended range of ejected electron angles, encompassing both the binary and recoil regions. The data show very strong correlations between the resonance amplitudes and the direct ionisation amplitudes.

1. Introduction

The (e, 2e) process, in which the kinematics of the electrons involved in an ionising collision are completely determined, is capable of revealing a rich variety of information. Depending on the kinematics employed, it is possible to investigate in detail either the ionisation mechanism itself or to use the reaction to elucidate the structure of the target system and the ion. When used to investigate structure, the technique is now generally known as electron momentum spectroscopy (EMS) and this application has recently been reviewed by McCarthy and Weigold (1988).

The present work reports several (e, 2e) studies of atoms carried out recently at Flinders University. These include the first measurements of the electron momentum distributions of an excited target state and the first measurements of the momentum distributions from an oriented target atom (Zheng *et al.*

* Paper presented at the Workshop on Interfaces in Molecular, Electron and Surface Physics, held at Fremantle, Australia, 4–7 February 1990.

0004-9506/90/040543$03.00

1990), the first direct measurement of d-wave correlations in the ground state of argon (McCarthy *et al.* 1989), and finally detailed measurements of correlations in the autoionising region of helium (Lower and Weigold 1990).

2. Electron Momentum Spectroscopy of Laser Excited Atoms

The application of the (e, 2e) process to electron momentum spectroscopy has been discussed in detail by McCarthy and Weigold (1976, 1988). Briefly if the incident and outgoing electron energies are E_0, E_1 and E_2 respectively, the electron separation or binding energy to a final state $|\psi_f\rangle$ is given by

$$\epsilon_f = E_0 - E_1 - E_2 . \tag{1}$$

The ion recoil momentum $\mathbf{k}$ is given by

$$\mathbf{k} = \mathbf{k}_0 - \mathbf{k}_1 - \mathbf{k}_2 , \tag{2}$$

whereas the momentum transfer $\mathbf{K}$, which is important in electron energy loss spectroscopy is defined by

$$\mathbf{K} = \mathbf{k}_0 - \mathbf{k}_1 \tag{3}$$

where $k_1 \geq k_2$ by convention.

For high incident energies and high momentum transfer collisions, the ionisation process can be considered as a binary encounter between the incident and ejected electron (McCarthy and Weigold 1976, 1988). Under these conditions the impulse approximation applies, and the EMS differential cross section is given by

$$\frac{d^5\sigma}{d\mathbf{k}_1 d\mathbf{k}_2 dE_2} = (2\pi)^4 \frac{k_1 k_2}{k_0} f_{ee} G_f(\mathbf{k}) , \tag{4}$$

where the electron-electron collision factor f_{ee} is the half-off-shell (to allow for the binding energy) Mott scattering cross section averaged over electron-spin degeneracies. In the noncoplanar symmetric geometry ($E_1 = E_2, \theta_1 = \theta_2$) the collision and kinematical factors are essentially independent of the angle $\phi = \pi - \phi_1 - \phi_2$ and the cross section is proportional to the structure factor $G_f(\mathbf{k})$, which for incident and outgoing plane waves (the plane wave impulse approximation PWIA) is given for atoms by

$$G_f(k) = (2J_0 + 1)^{-1} \sum_{M_0 M_f} |\langle \mathbf{k}\Psi_f : J_f M_f | \Psi_0 : J_0 M_0 \rangle|^2 , \tag{5}$$

where the sum over final-state electronic degeneracies and an average over initial-state electronic degeneracies is taken, and $|\Psi_0\rangle$ and $|\Psi_f\rangle$ are the N and $(N-1)$ electron initial and final states respectively. By measuring the cross section as a function of $\mathbf{k}$ it is possible to measure the square of the (one electron) overlap function $\langle \Psi_f | \Psi_0 \rangle$ in momentum space. This is the probability that the observed ion state $|\Psi_f\rangle$ is obtained by annihilating an electron of momentum $-\mathbf{k}$ and spin coordinate σ in the target state $|\Psi_0\rangle$. In second quantised notation the operator that annihilates such an

electron is $\Sigma_{j\alpha m}\phi^j_{\alpha m}(\mathbf{k},\boldsymbol{\sigma})\mathbf{a}^j_{\alpha m}$. The function $\phi^j_{\alpha m}$ is the single particle orbital in momentum-spin space for total angular momentum j with projection m. The remaining quantum numbers are denoted by α (e.g. principal quantum number for an atomic orbital). The radial factor of $\phi^j_{\alpha m}(\mathbf{k},\boldsymbol{\sigma})$ is denoted $\phi^j_\alpha(k)$. The structure factor (5) can then be written (McCarthy and Weigold 1988)

$$G_f(k) = (2J_0+1)^{-1} \sum_{j\alpha\beta} \phi^j_\alpha(k)\phi^j_\beta(k)\langle \Psi_0 \| a^{j\dagger}_\alpha \| \Psi_f\rangle \cdot \langle \Psi_f \| a^j_\beta \| \Psi_0\rangle . \tag{6}$$

The dot product in (6) denotes the scalar product of tensor operators

$$\mathbf{a}^j_\alpha \cdot \mathbf{a}^j_\beta = \Sigma_m a^\dagger_{\alpha m} a^j_{\beta m} . \tag{7}$$

There is a manifold of states $|\Psi_f\rangle$ that contain the one-hole configuration resulting from the annihilation of an electron in the characteristic orbital $\phi^j_\alpha(k)$ in $|\Psi_0\rangle$. One can define the manifold structure factor $W_{j\alpha}(k)$ by summing over all final states belonging to the manifold characterised by $j\alpha$:

$$W_{j\alpha}(k) = \sum_{f\epsilon j\alpha} G_f(k) = (2J_0+1)^{-1} \sum_{i\mu\nu} \phi^i_\mu(k)\phi^i_\nu(k)\langle \Psi_0 | \mathbf{a}^{i\dagger}_\mu \cdot \mathbf{a}^i_\nu | \Psi_0\rangle . \tag{8}$$

This sum is dominated by the term $i=j, \mu=\nu=\alpha$, hence the manifold structure factor is labeled by j,α. The last factor is the target ground state density matrix obtained by a structure calculation and it can be sensitive to details in different many-body calculations of the ground state $|\Psi_0\rangle$.

The spectroscopic factor or pole strength $S_{f,j\alpha}(k)$ for the one-hole manifold $j\alpha$ is given by

$$G_f(k) = S_{f,j\alpha}(k) W_{j\alpha}(k) . \tag{9}$$

It is obvious that the spectroscopic factors obey the sum rule

$$\sum_{f\epsilon j\alpha} S_{f,j\alpha}(k) = 1 . \tag{10}$$

For closed-shell targets it is usually reasonable to neglect electron correlations and to make the target Hartree-Fock approximation (THFA) in which $|\Psi_0\rangle = |\Phi_0\rangle$ the Hartree-Fock configuration for the target. In this case the structure factor simplifies to

$$G_f(k) = (2j+1) S_{f,j\alpha} [\phi^j_\alpha(k)]^2 . \tag{11}$$

and the spectroscopic factor is now independent of momentum. The spectroscopic factor in the THFA is simply the probability that $|\Psi_f\rangle$ consists of a hole in $|\Phi_0\rangle$ with quantum numbers j,α.

Zheng *et al.* (1990) recently reported the first (e, 2e) measurements made on a target in an excited state and the first measurements made on an oriented target. This was achieved by measuring the (e, 2e) cross section for sodium atoms pumped by σ^+ laser light tuned to the $3^2S_{1/2}(F{=}2) \leftrightarrow 3^2P_{3/2}(F'{=}3)$ transition. The excited pumped atoms were in the $m_{F'}=3$ state, or in terms

of orbital momentum in the $m_\ell = +1$ state. The coordinate frame was chosen so that the electron momentum density of the excited state was probed in the k_x direction with k_z and k_y being fixed and essentially zero.

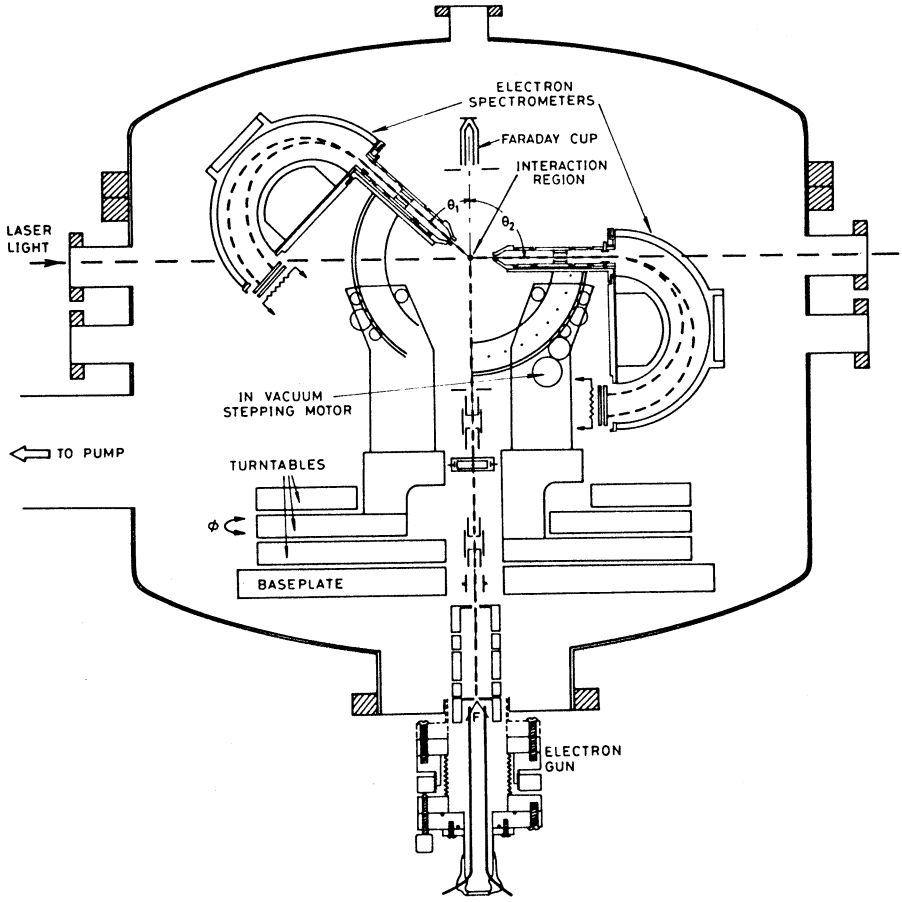

Fig. 1. Schematic view of the (e, 2e) coincidence spectrometer. The electron beam, laser beam, and sodium atom beam intersect at right angles. The sodium oven (not shown) is mounted perpendicular to the plane of the diagram. In the measurements $\theta_1 = \theta_2 = 45°$ and ϕ is varied.

A schematic view of the apparatus used is shown in Fig. 1 and of the associated circuitry in Fig. 2. The sodium oven, which produces the well collimated sodium beam, is mounted out-of-the-plane of Fig. 1 at right angles to the intersecting horizontal laser beam and vertical electron beam. In these EMS measurements noncoplanar symmetric kinematics was used, i.e. the polar angles θ_1 and θ_2 were both kept fixed at 45°, and the out-of-plane azimuthal angle ϕ of one of the spectrometers was varied. The incident electron energy was 804 eV, and the outgoing energies of both detected electrons was in the range 400 ± 4 eV. The experimental energy resolution function and the angular resolution of the spectrometer were established by careful measurements of

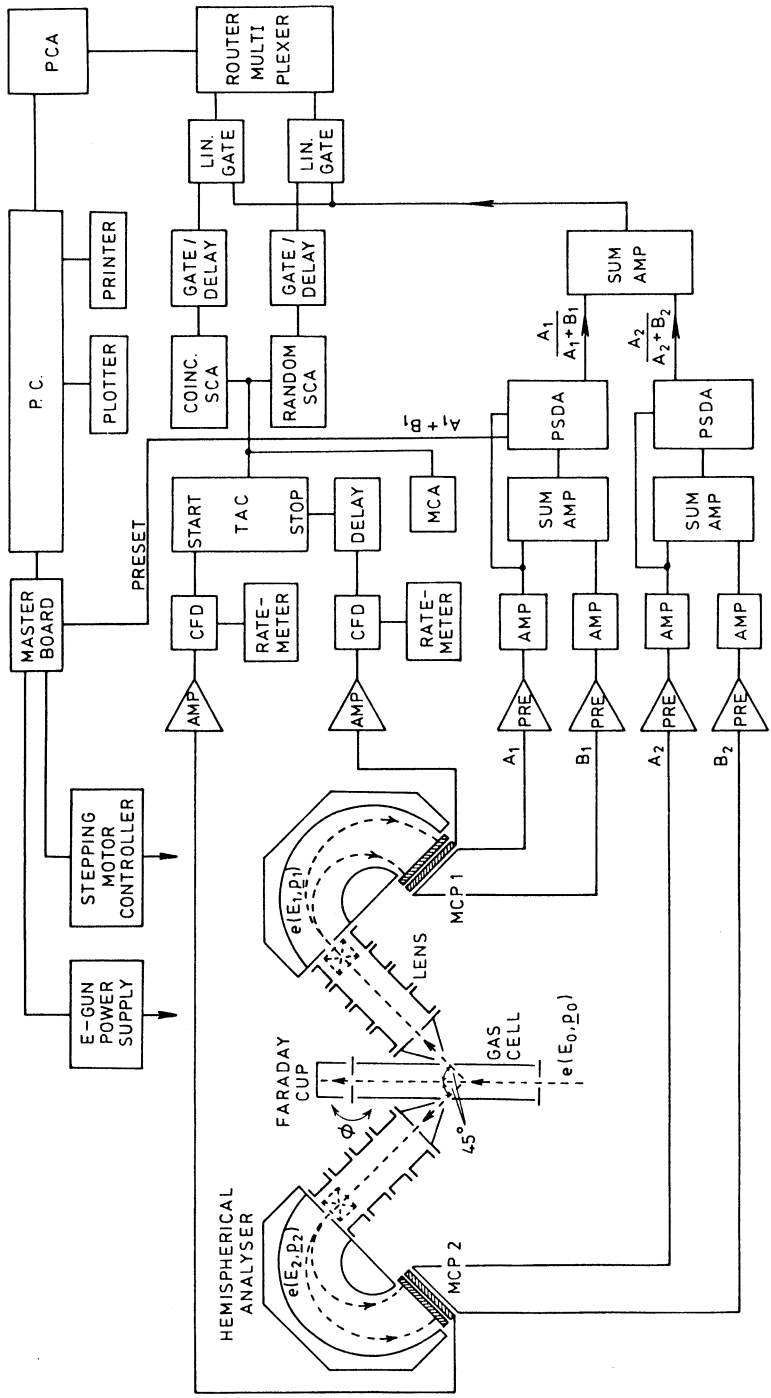

Fig. 2. The coincidence and energy determining circuitry. The energy determination is made by the position decoding electronics (PSDA). The measurements are made as a function of $\epsilon = E_0 - (E_1 + E_2)$ and the out-of-plane azimuthal angle ϕ.

the argon 3p separation energy spectrum and its angular correlation. The angular resolution was $\Delta\theta \approx 1°$, $\Delta\phi \approx 0 \cdot 5°$.

Fig. 2 shows the fast timing logic and the circuitry used for determining true coincidence events and the energies of the corresponding electrons. The coincidence spectrometer is based on two hemispherical electron energy analysers with position sensitive detectors sensitive in the energy dispersing dimension (Zheng 1989). It is similar in principle to the noncoplanar symmetric spectrometer described by McCarthy and Weigold (1988). The energy determination is based on the fact that the radial exit position for an electron passing through a hemispherical analyser is proportional to its entrance energy (e.g. Lower and Weigold 1989). This exit position is obtained from a resistive anode by measuring the division of charge emitted by the microchannel plates mounted at the exit plane of the analyser. A general description of the technique is given by McCarthy and Weigold (1988) and Weigold and Zheng (1990). The whole experiment is under computer control.

Fig. 3 shows the optical arrangement used. An argon ion laser pumps a tunable CW ring dye laser whose light is then right-hand circularly polarised. A split photodiode is used to keep the laser tuned to the $3^2S_{1/2}$(F=2) $\rightarrow$ $3^2P_{3/2}$(F′=3) transition for atoms in the narrow sodium beam. A beam expander, consisting of two lenses and an aperture A1 is inserted in the beam, so that only a narrow section of the beam is used, creating a semi-constant radiation intensity across the pump region. In this way uncertainty due to the gaussian profile of the pump laser is avoided. In the stationary condition this pumping with σ^+ light produces a population of the F = 2, $m_F = 2$ ground state with about 12% of the beam in the $F' = 3$, $m_{F'} = 3$ excited state. This means that in the excited state there is no population in the $m_l = 0$ (i.e. $3p_z$) orbital, all being in the $m_l = +1$ state, corresponding to 50% in both the $3p_x$ and $3p_y$ orbital. The axis of quantisation z has been chosen as being the direction of propagation of the circularly polarised pumping beam, the atomic sodium beam is incident in the x direction and the electron beam is incident in the y direction. This is shown schematically in Fig. 4, which also shows the $3p_x$ and $3p_y$ distribution of the charge cloud of the sodium in the $3p(m_l = +1)$ excited state. The scattering plane is the zy plane and both outgoing electrons make a polar angle of 45° with respect to the incident (y) direction, the out-of-plane azimuthal angle ϕ of electron 2 is varied to probe the different momentum components of the target (see Fig. 1). Thus the experiment measures the (e, 2e) triple differential cross section as a function of the x component of momentum, k_x. For the symmetric noncoplanar kinematics employed, the z and y components of momenta are fixed and essentially zero for $\theta_1 = \theta_2 = \theta = 45°$ and small binding energies. Due to the finite angular and hence momentum resolution of the spectrometers, the average values of $|k_y|$ and $|k_z|$ are not quite zero, being of the order of $0 \cdot 06$ a.u.

Fig. 5 shows the results obtained for the excited state $3p(m_l = 1)$ momentum distribution compared with the momentum distribution given by the Hartree-Fock $3p(m_l = +1)$ wavefunction. The finite angular (i.e. momentum) resolution has been included in the calculations. The main effect of the finite angular resolution is to fill in the momentum distribution at momenta close to zero. The momentum distribution peaks at very small momenta ($\sim 0 \cdot 2$ a.u.) because of the diffuse nature of the 3p orbital in coordinate space. Also shown in the

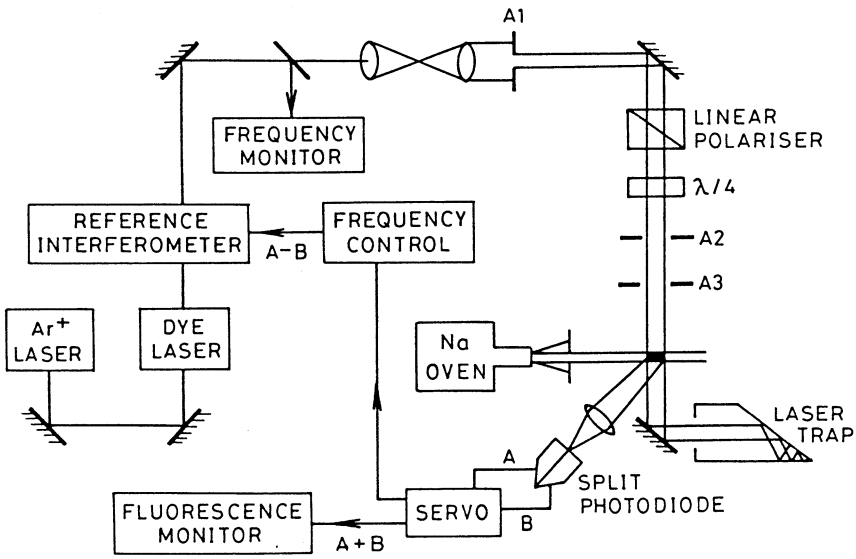

Fig. 3. The arrangement of the optical system. For details see text.

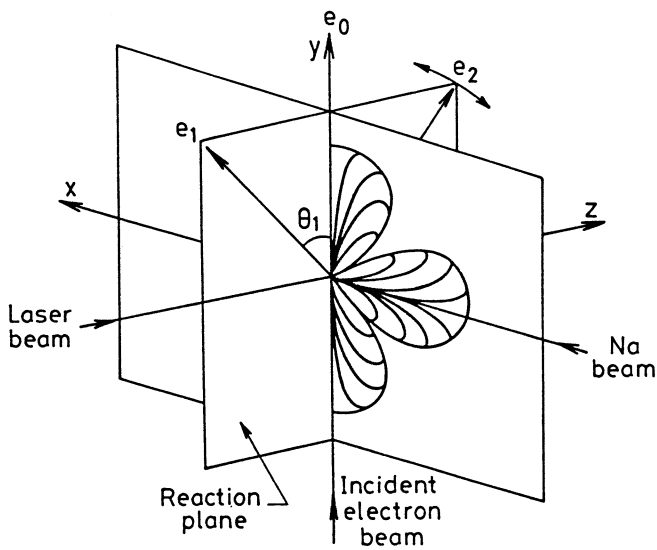

Fig. 4. Schematic diagram of the experimental geometry. The $3p_x$ and $3p_y$ charge cloud distributions are indicated. The polar angles are $\theta_1 = \theta_2 = 45°$. The out-of-plane azimuthal angle ϕ of detector 2 is varied to vary the momentum k_x.

figure for comparison is the momentum distribution expected for the $m_l = 0$ substate of the 3p state. That for the unoriented $3p_{(0,\pm1)}$ state is similar to that for the $m_l = 1$ substate, but in significantly poorer agreement with the data due to the inclusion of the $m_l = 0$ component. The momentum distribution for the $m_l = 0$ (i.e. $3p_z$) state is of course zero along the k_x axis ($k_y = k_z = 0$), since the $3p_z$ (dumbbell) orbital is perpendicular to the nodal $x-y$ plane, the node being at the origin. However, due to the finite momentum resolution, there is a finite probability of seeing some $m_l = 0$ contribution, this probability decreasing as one moves away from the origin along the k_x (or for that matter the k_y) direction. This explains the "anomalous" shape of the expected $m_l = 0$ ($3p_z$) momentum distribution along the k_x axis.

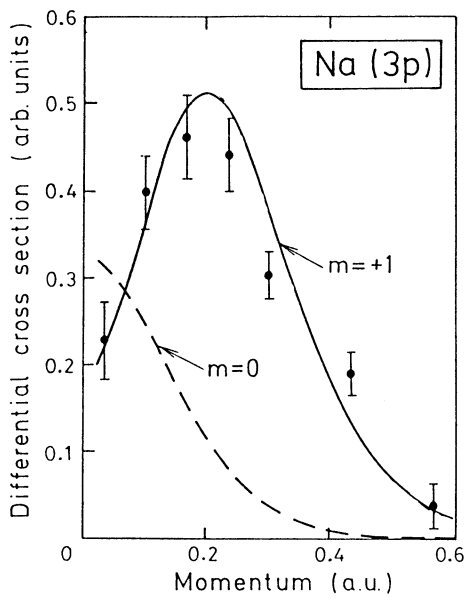

Fig. 5. The measured and calculated momentum profiles for the excited 3*p* state of sodium (Zheng *et al.* 1990). The solid curve is the calculated $3p(m_l = +1)$ profile and the long dashed curve that expected for the $m_l = 0$ component. The PWIA calculations use a HF 3p wave function with the experimental angular resolution folded in. The momentum is probed along the k_x axis.

3. Electron Momentum Spectroscopy of Argon

The structure of argon and its ion has been a central problem in atomic structure theory for some time (McCarthy and Weigold 1976, 1988). It contains all the complications of initial state and final state correlations in a case where many of the final states below the double ionisation continuum can be experimentally resolved. In addition there are two occupied valence states, 3p and 3s, in the target Hartree-Fock configuration of the ground state, so that it is possible to test the consistency of the spectroscopic factor determination in EMS using two methods of normalisation, the spectroscopic sum rule (equation 10) and comparison of the structure factor with the manifold structure factor for a different manifold, namely the 3p and 3s manifolds (equation 8).

The outer valence 3p manifold is dominated by the transition to the ground state of the ion. McCarthy *et al.* (1989) recently measured the spectroscopic factor for this transition to be $0\cdot95 \pm 0\cdot02$. Its momentum profile shape at 1500 eV is described within experimental error by the distorted wave impulse approximation (DWIA), and up to $k \sim 1\cdot7$ a.u. by the plane wave impulse

approximation (PWIA) using the HF 3p wave function to describe the struck electron (see Fig. 6). In the high momentum region, above $k \sim 1 \cdot 7$ a.u., the PWIA significantly underestimates the cross section. McCarthy *et al.* (1989) normalised their measured cross sections at $\phi = 10°$ to the $3p^{-1}$ DWIA cross section for the ground state transition obtained by multiplying the calculated $3p^{-1}$ manifold cross section by the ion ground state spectroscopic factor of $0 \cdot 95$ (equations 8 and 9). In order for the PWIA cross section to agree with the DWIA value at this point it has to be multiplied by $0 \cdot 83$, the PWIA cross section being larger than the DWIA one since it neglects refraction of the electron waves.

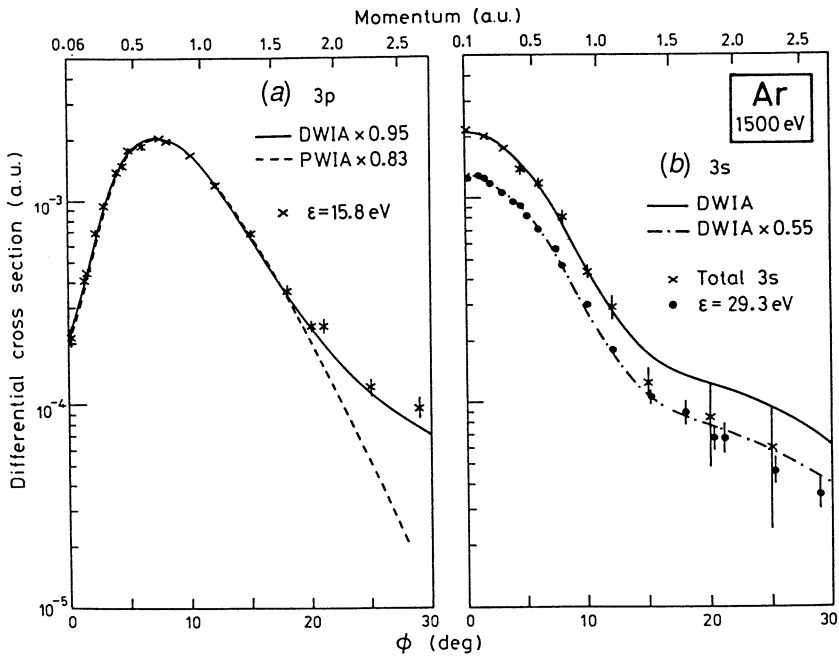

Fig. 6. The 1500 eV noncoplanar symmetric momentum profiles for the Ar ground state transition ($\epsilon = 15 \cdot 8$ eV), first excited state ($\epsilon = 29 \cdot 3$ eV), and the total $^2S^e$ manifold compared with the DWIA and PWIA cross sections using (*a*) HF 3p and (*b*) HF 3s wavefunctions. All the data have been normalised by fitting the measured ground state cross section to $0 \cdot 95$ times the 3p DWIA cross section, the spectroscopic factor for the ground state transition being $0 \cdot 95$ (McCarthy *et al.* 1989).

The 3s manifold on the other hand has a number of states with significant spectroscopic strength, the separation energy spectra showing a lot of structure extending above the double ionisation threshold at $43 \cdot 6$ eV (Weigold *et al.* 1973; McCarthy and Weigold 1976, 1988; McCarthy *et al.* 1989). The shapes of the different momentum profiles for the strongly excited states at large separation energy, and also that of the continuum above the double ionisation threshold, are independent of energy and have the characteristic shape of 3s momentum distributions up to a little over 1 a.u. of momentum. Fig. 6*b* shows that the distorted wave impulse approximation with the target Hartree-Fock 3s momentum distribution (DWIA-THFA) describes the shape and normalisation of the whole $^2S^e$ manifold structure factor for all momenta (or ϕ). The

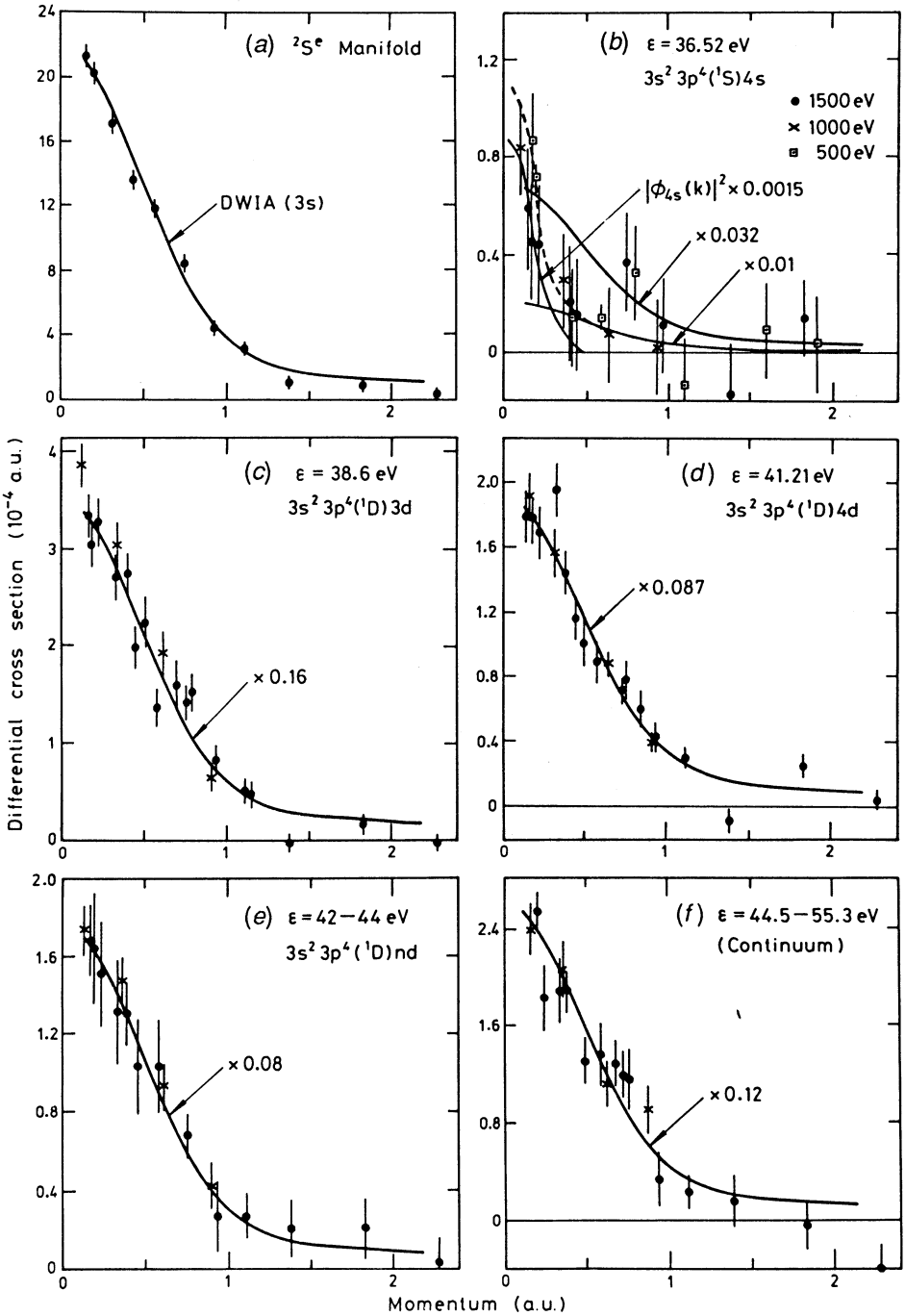

Fig. 7. Momentum profiles for the $^2S^e$ manifold of argon and various satellites compared with the calculated 3s momentum profiles multiplied by their respective spectroscopic factors (McCarthy *et al.* 1989). The dominant configurations for the corresponding ion states and the respective separation energies are as shown. The dominant $^2S^e$ transition to the $3s3p^6$ ion state at $\epsilon = 29 \cdot 3$ eV is shown in Fig. 6*b*. For the $3s^2 3p^4 4s$ transition a 4s HF momentum profile scaled by the factor $0 \cdot 0015$ is also shown in Fig. 7*b*.

cross section for the transition at 29·3 eV with dominant ion configuration $3s3p^6(^2S^e)$ is also well described by the DWIA-THFA using a spectroscopic factor of 0·55. The momentum profiles for other $^2S^e$ final states, as well as the contributions in the range 42–55 eV, are shown in Fig. 7. They are accurately described by the calculated 3s profile, except that for the 36·52 eV ion state with dominant configuration $3s^23p^4(^1S)4s$, which shows a sharp peak below 0·3 a.u. of momentum. The extra strength at low momentum can be explained by 4s ionisation with a spectroscopic factor of about 0·0015 due to a small $3s^23p^4(^1S)4s^2$ component in the argon ground state. The spectroscopic factors for the $^2S^e$ manifold are found to be independent of energy in the range 500–1500 eV. They are also independent of momentum in the range 0–2 a.u. except that for the $3s^23p^44s$ state discussed above, where initial state correlations are important.

Table 1. Spectroscopic factors for the $^2S^e$ manifold of argon compared with calculated values

The experimental values are independent of momentum k in the range 0–2 a.u. except for the $3p^44s$ transition, indicated by an asterisk, where S_f decreases from 0·03±0·01 at $k <$ 0·2 to 0·01 ± 0·01 at $k >$ 0·5 a.u. The error in the last figure is given in parentheses

Dominant ion state configuration	Experiment EMS[A] ϵ (eV)	S_f	Spectroscopic factor S_f Overlap[B]	FSCI[B]	FSCI[C]	GF[D]	GF-ADC(4)[E]
$3s3p^6$	29·24	0·55(1)	0·649	0·600	0·618	0·553	0·605
$3p^44s$	36·50	0·02(1)*	0·013	0·006	0·006		0·008
$3p^43d$	38·58	0·16(1)	0·161	0·142	0·112	0·199	0·135
$3p^44d$	41·21	0·08(1)	0·083	0·075	0·057	0·107	0·005
$3p^45d$	42·65				0·021	0·042	0·025
	]	0·08(1)	0·081	0·095			
$3p^46d$	43·40				0·009	0·021	
$Ar^{++}+\epsilon$		0·12(1)	0·013	0·08	0·18	0·076	0·177

[A] McCarthy *et al.* (1989). [B] Mitroy *et al.* (1984). [C] Hibbert and Hansen (1987).
[D] Amusia and Kheifets (1985, 1990). [E] Von Niessen (1987).

Table 1 compares the spectroscopic factors for the $^2S^e$ manifold obtained in a number of many-body calculations with those measured by McCarthy *et al.* (1989), which are consistent with earlier less accurate EMS measurements (see for example McCarthy and Weigold 1976, 1988). The final state configuration interaction (FSCI) calculations include only final state correlation, whereas the overlap and the Green's function (GF) calculations include initial state correlations and relaxation as well as final state correlations. None of the calculations adequately describes the data, although those of Amusia and Kheifets (1985, 1990) obtain the correct spectroscopic factor for the main transitions.

Since initial state correlations play a very small role in the $^2S^e$ manifold, the energy of the 3s orbital may be obtained using the weighted mean of final states belonging to the $^2S^e$ manifold (McCarthy and Weigold 1976). The result is $\epsilon_{3s} = 35·2 \pm 0·2$ eV, which compares very well with the HF value of 34·76 eV.

Although the dominant features in the argon separation energy spectra above the $^2P^o$ $3s^23p^5$ ion ground state at 15·76 eV and the $^2S^e$ $3s3p^6$ ion excited state at 29·3 eV are due to transitions to other states belonging to the $^2S^e$ manifold, McCarthy *et al.* (1989) were able to identify transitions belonging

to both the $^2D^e$ and $^2P^o$ manifolds. The $^2D^e$ transitions can only occur if there are d-wave correlations in the Ar ground state. The most prominent $^2D^e$ transition is to the $3s^23p^4(^1D)$ 4s state at 34·20 eV, and its momentum profile, shown in Fig. 8*a*, is very interesting. It has a narrow peak at $k \sim 0{\cdot}25$ a.u., which is to be expected from the diffuse (in coordinate space) spectroscopic 3d and 4d orbitals. The Hartree-Fock 3d and 4d momentum distributions are shown in Fig. 8*a* multiplied by the normalisation factors indicated, which must be less than or equal to the square of the corresponding CI expansion coefficient for the d-wave configurations in the argon ground state. The low momentum region is best described by the 4d wave function. If the intensity of the low momentum peak is attributed to say a ground state $3s^23p^4(^1D)4s4d$ configuration, it would require only a 0·4% admixture of this configuration in the argon ground state to account for its intensity.

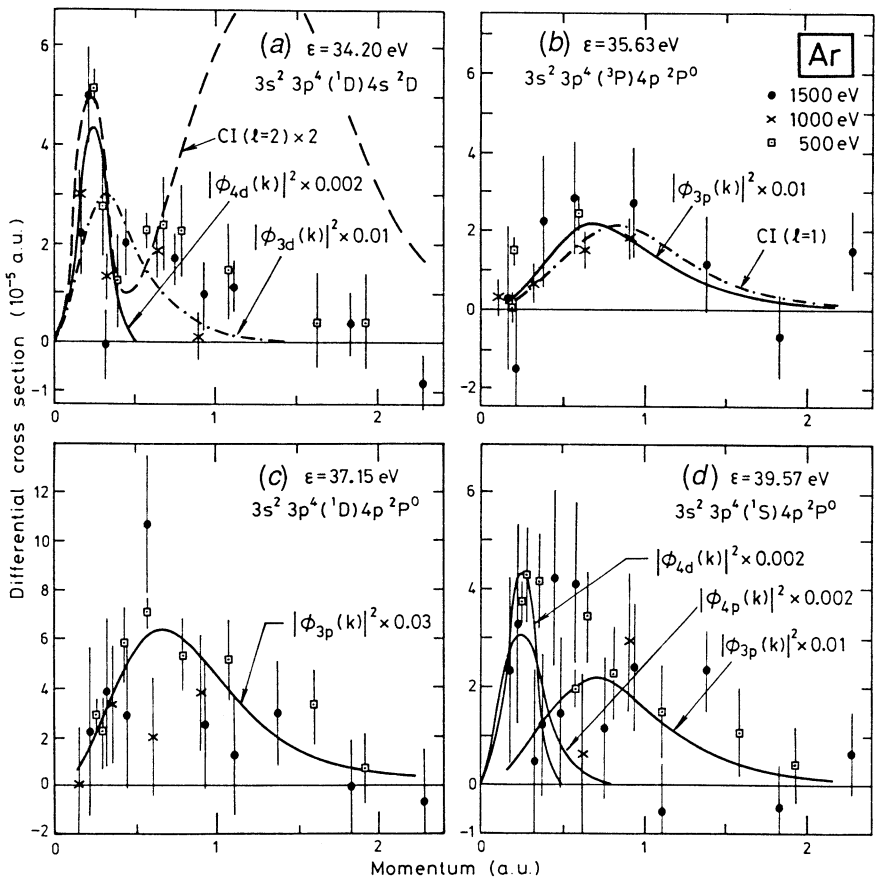

Fig. 8. The momentum profiles to final states at (*a*) 34·2, (*b*) 35·6, (*c*) 37·15 and (*d*) 39·6 eV separation energy compared with several calculated distributions (McCarthy *et al.* 1989). The factors following the 3p calculated distributions are 3p spectroscopic factors. The CI($l = 2$) distribution is the total $^2D^e$ manifold distribution obtained by Mitroy *et al.* (1984). The CI($l = 1$) distributions are 0·67 of the total $^2P^o$ satellite distribution obtained by Mitroy *et al.* The 3d, 4d and 4p distributions shown are the spectroscopic Ar 3d, 4d and 4p momentum distributions with their respective spectroscopic strengths.

Dyall (1980) carried out a CI calculation of the argon ground state including double excitations of the form $(nl)^2$ with $n = 3$ and 4. He found that the major interaction in the argon ground state involved the d-wave configurations. The total d-wave strength given by the Dyall calculation is a factor of 3 higher than that observed for the 34·20 eV transition by McCarthy *et al.* (1989). Dyall's calculation does not predict any detectable cross section above $k \sim 0{\cdot}5$ a.u., in disagreement with the measurements. Mitroy *et al.* (1984) carried out a full calculation of the overlap function between the correlated Ar ground state and correlated final states. The $^2D^e$ manifold momentum distribution calculated by Mitroy *et al.* is shown in Fig. 8*a* multiplied by a factor of 2. Clearly this calculation underestimates the intensity of the small momentum peak and overestimates the contributions at high momentum. Mitroy *et al.* found that the dominant contribution of the correlation energy came from "correlating" pseudo-natural orbitals rather than the spectroscopic (Hartree-Fock) orbitals. These pseudo-orbitals are localised in the same region of space as the spectroscopic 3s and 3p orbitals and therefore give rise to momentum contributions at much higher momenta than those given by the diffuse spectroscopic 3d and 4d orbitals. The measurements of McCarthy *et al.* (1989) show that the spectroscopic 4d orbital is more important than given by the calculation of Mitroy *et al.* who overestimate the large momentum components due to the 3d pseudo-orbital.

The transition at $\epsilon = 39{\cdot}6$ eV also has a very similar momentum distribution to that for the $3s^23p^4(^1D)4s\ ^2D^e$ state (Fig. 8*d*). This could be due to excitation of the $3s^23p^4(^3P)4d\ ^2D^e$ ion state at 39·64 eV. Some of the cross section is also probably due to the excitation of the $3s^23p^4(^1S)4p\ ^2P^o$ ion state at 39·57 eV. Although the low momentum region cannot be explained by a 3p ionisation process, there could be a 4p contribution from the $3s^23p^4(^1S)4p^2$ component in the Ar ground state.

McCarthy *et al.* (1989) find two definite $^2P^o$ transitions (Figs 8*b* and 8*c*) in addition to the dominant ground state transition. Both transitions have the 3p momentum distribution. Shown in Fig. 8*b* are both the 3p DWIA-THFA momentum distribution multiplied by the spectroscopic factor of 0·01, and 0·67 of the total $^2P^o$ satellite intensity calculated by Mitroy *et al.* (1984) in their full overlap calculation marked CI(l=1). There is a small difference in shape between the HF and CI calculations due to the effect of initial state correlations. Both describe the data adequately. The spectroscopic factors are 0·01 and 0·03 for the 35·63 and 37·15 eV transitions respectively. The observed spectroscopic factors in the $^2P^o$ manifold are in very good agreement with a number of many-body calculations (McCarthy *et al.* 1989).

4. (e,2e) Coincidence Measurements in the Autoionising Region of Helium

The autoionisation of atoms excited by electron impact involves in general the interference between the direct-ionisation amplitude and the resonance or autoionisation amplitude. This interference depends on the momenta of the scattered and ejected electrons. Most of the recent work on electron impact autoionisation has concentrated on observing the resonance profiles as a function of the angle of either the ejected or scattered electron. The "ejected" electron is by convention taken to be the electron whose energy

corresponds to the difference between the energy of the autoionising state and that of the residual ion, and the "scattered" electron is taken to be the other free electron in the final state even though its energy may be lower than that of the ejected electron. Experiments which involve the detection of only one of the emitted electrons always involve integration over the momenta of the undetected electrons.

On the other hand, the measurement of (e, 2e) cross sections in the region of an autoionising resonance gives information on the resonance and direct cross section amplitudes as well as on their relative phases, i.e. their interference, as a function of the momenta $\mathbf{k}_e$ of the ejected electron for known values of the momentum transfer $\mathbf{K} = \mathbf{k}_o - \mathbf{k}_s$, where $\mathbf{k}_o$ and $\mathbf{k}_s$ are the momenta of the incident and scattered electrons respectively.

Therefore (e, 2e) cross section measurements in the autoionising region can provide very sensitive information on details of the excitation process of the resonance as well as on the interference in the decay channel with direct ionisation. For instance, in the absence of a direct contribution and interference between excitation amplitudes to the various magnetic substates of the resonance, the angular correlations between the scattered and ejected electrons should have the form $[P_\ell(\cos\theta')]^2$ in the scattering plane for an electron emitted with angular momentum l, where θ' is the angle of emission relative to the symmetry axis $\mathbf{K}$ (Balashov *et al.* 1971, 1972). Deviations from such a distribution are due to interference between excitation amplitudes of the different magnetic substates of the resonance as well as to interference between amplitudes for direct and resonant ionisation. Since the description of the process also depends on an accurate knowledge of the wavefunction of the doubly excited autoionising process, the technique provides a sensitive measure of the correlations between the excited electrons.

For separable resonances, i.e. if resonances of the same LS do not overlap, and if there is no appreciable interaction between the two final state electrons, Tweed (1976) showed that the triple differential (e, 2e) cross section in the vicinity of the rth autoionising resonance can quite generally be written in the parametrised form originally due to Shore (1967):

$$\frac{d^5\sigma}{d\Omega_e d\Omega_s dE_e} = f(\mathbf{k}_e, \mathbf{K}) + \sum_\mu \frac{a_\mu(\mathbf{k}_{e\mu}, \mathbf{K}_\mu)\epsilon_\mu + b_\mu(\mathbf{k}_{e\mu}, \mathbf{K}_\mu)}{1+\epsilon_\mu^2}, \tag{12}$$

where

$$k_{e\mu}^2 = 2\bar{E}_\mu, \tag{13}$$

$$\epsilon_\mu = 2(E_e - \bar{E}_\mu)\Gamma_\mu^{-1}, \tag{14}$$

and $\bar{E}_\mu$ and E_μ are respectively the energies of the rth autoionising resonance and the energy of the ion plus continuum emitted electron (relative to the energy of the residual ion) with total angular momentum and spin quantum numbers denoted by $\mu = \{r; L, M, S\}$. The energy full width at half maximum of the resonance is given by Γ_μ.

The momentum dependent parameters a_μ and b_μ have dimensions of cross sections and are related to the resonance contributions and the form of the

resonance profiles, whereas f is simply the cross section for direct ionisation. Further, a_μ is a measure of the asymmetry of the resonance profile and b_μ of its contributions to the triple differential cross section at the position $\bar{E}_\mu$ of the resonance state. We use the subscript r to designate that the sum over magnetic substates has been made for a separate resonance r of given LS.

The parameters a_μ and b_μ depend upon matrix elements which contain both the direct and resonance amplitudes, the resonance amplitudes being essentially given by the probability of transfer of momentum to the atomic target multiplied by the probability for subsequent decay into the continuum. The sum is over terms arising from the different products of incident and scattered electron partial waves and includes the appropriate phase factors and angular dependent spherical harmonics. The expressions for the parameters a_μ and b_μ and f derived by Tweed (1976) are

$$a_\mu(\mathbf{k}_e,\mathbf{K}) = 2\frac{\mathbf{k}_e}{\mathbf{k}_o}(2S+1)Re\sum_{\mu_e} I^*_{\mu_e}(\mathbf{k}_e,\mathbf{K})\delta_{S,S_e}[J_\mu(\mathbf{k}_e,\mathbf{K})(\pi V_{\bar{E}_\mu})^{-1} - iI_\mu(\mathbf{k}_e,\mathbf{K})], \tag{15}$$

$$b_\mu(\mathbf{k}_e,\mathbf{K}) = \frac{\mathbf{k}_e}{\mathbf{k}_o}(2S+1)\{(|J_\mu(\mathbf{k}_e,\mathbf{K})(\pi V_{\bar{E}\mu})^{-1}|^2 + |I_\mu(\mathbf{k}_e,\mathbf{K})|^2 + 2Im\sum_{\mu_e} I^*_{\mu_e}(\mathbf{k}_e,\mathbf{K})\delta_{S,S_e}[J_\mu(\mathbf{k}_e,\mathbf{K})(\pi V_{\bar{E}_\mu})^{-1} - iI_\mu(\mathbf{k}_e,\mathbf{K})]\} \tag{16}$$

and

$$f(\mathbf{k}_e,\mathbf{K}) = \frac{2\mathbf{k}_e}{\mathbf{k}_0}\sum_S(2S+1)|\sum_{LM} I_{LMS}(\mathbf{k}_e,\mathbf{K})|^2, \tag{17}$$

where

$$V_{\bar{E}_\mu} = \langle \psi_c^{0ke^*_\mu} | H_t | \psi_b^\mu \rangle, \tag{18}$$

$$\Gamma_\mu = 2\pi | V_{\bar{E}_\mu} |^2 . \tag{19}$$

Here H_t is the target Hamiltonian and the wavefunctions ψ_b^μ and $\psi_c^{0ke_\mu}$ are defined to be respectively the wavefunctions of the rth autoionising state of energy $\bar{E}_\mu$ and the ion plus continuum electron of energy E_e. Further, I_μ and J_μ are matrix elements of the interaction potential between the initial state wavefunction and the final state wavefunction, which are a product of a free electron function representing the scattered electron and the wavefunctions $\psi_c^{0ke_\mu}$ and ψ_b^μ respectively. The direct cross section depends on the square of the direct ionisation amplitudes I_μ, and the resonance parameters a_μ and b_μ depend on both I_μ and J_μ and their relative phases. In expressions (15) and (16) the excitation and the decay of the autoionising states are treated independently. The J_μ express the probability of transfer of momentum to the target, the subsequent decay into the continuum appearing in the $V_{\bar{E}_\mu}$.

Figs 9 and 10 provide some examples of the observed coincidence ejected electron spectra obtained from the present series of experiments. The ejected electron angles for the azimuths $\phi_e = 0$ and $\phi_e = \pi$ are indicated by the angles θ_e and $-\theta_e$ respectively (where $\phi_s = 0$). In each case we see a series

of resonance profiles superimposed upon a background of direct ionisation events. The final fitted function (12) is represented by the solid curve, whilst the fitted direct ionisation background f and the individual fitted resonance profiles $(a\epsilon+b)/(\epsilon^2+1)$ convoluted with the instrumental response, are indicated by dashed lines.

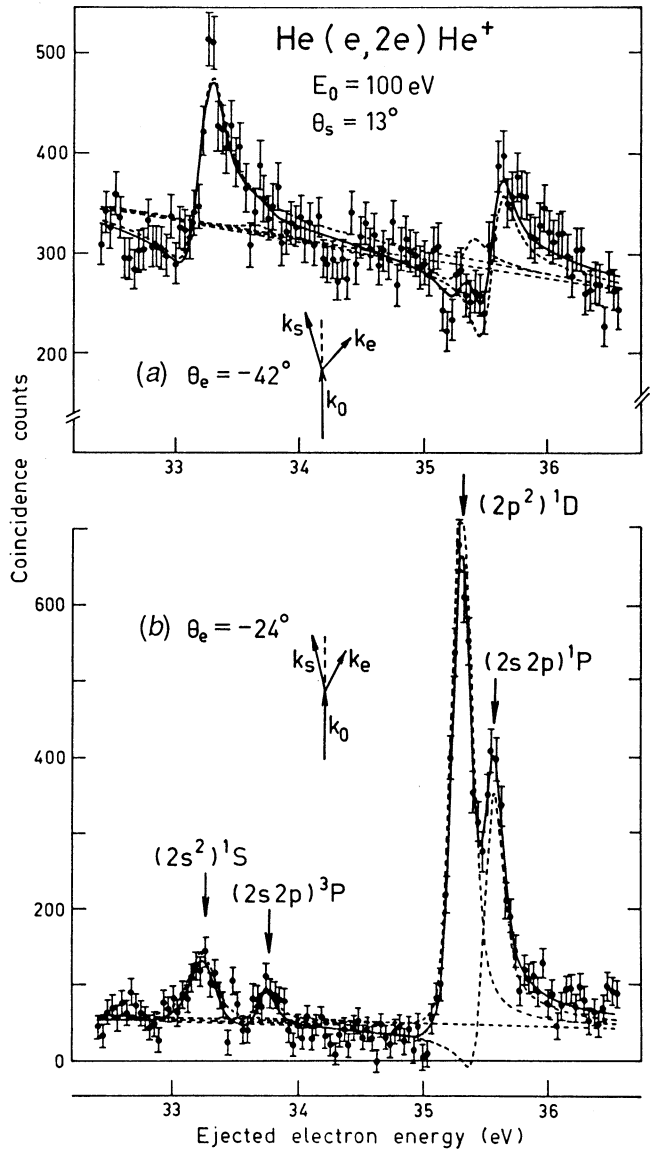

Fig. 9. Selected coincidence ejected electron spectra for He(e, 2e)He$^+$ at an incident energy of 100 eV and scattering angle of 13° for (*a*) $\theta_e = -42°$ and (*b*) $\theta_e = -24°$. The momenta of the electrons are indicated. The dashed curves show the convoluted parametric fits of equation (12) to the individual resonances and direct background, and the solid curve the resultant overall fit to the data (Lower and Weigold 1990).

Figs 9*a* and 9*b* were obtained at an incident energy of 100 eV and with the scattered electron analyser fixed at 13° with respect to the incident beam direction. These spectra were collected in the binary collision region ($\phi_e = \pi$, $\phi_s = 0$), where scattered and ejected electrons are detected on opposite sides of the incident beam. The spectrum of Fig. 9*b* was collected at an ejection angle of −24°, and shows a case where the direct ionisation cross section is small and the resonance profiles fairly symmetric. Fig. 9*a* shows the equivalent coincidence spectrum obtained with an increase in ejection angle of only 18°. It illustrates dramatically how sensitively the cross sections for direct and

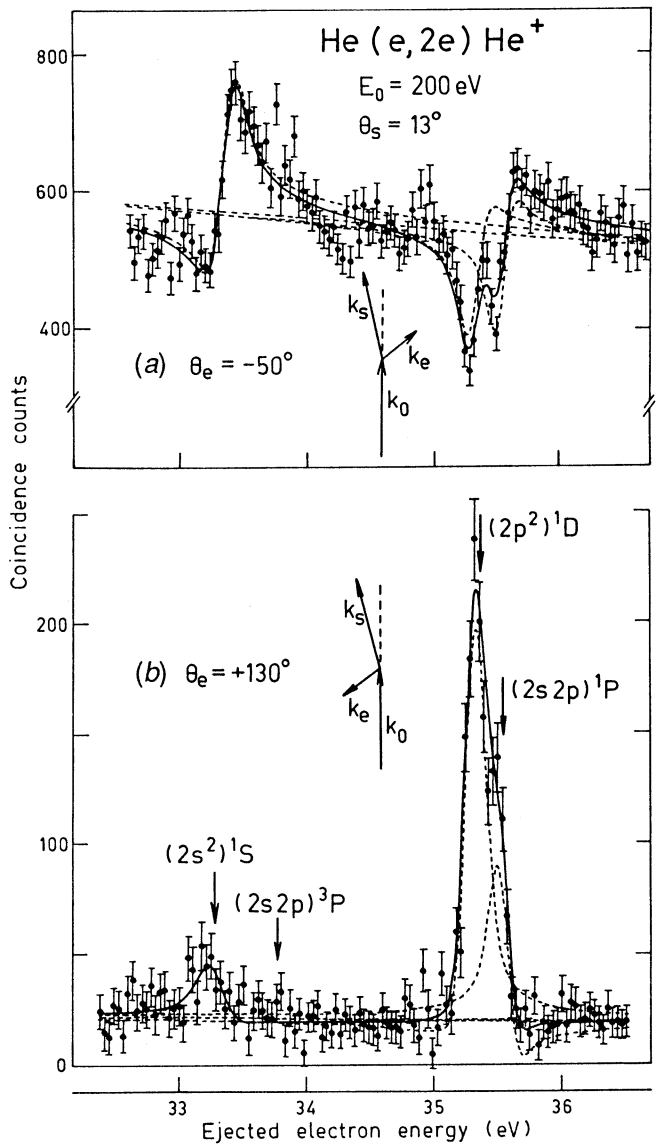

Fig. 10. Selected coincidence ejected electron spectra for He(e, 2e)He$^+$ at 200 eV incident energy and for a scattering angle of 13°. Details as in Fig. 9.

resonant ionisation depend upon the value of ejected electron momentum. Most marked is the reduction in intensity of the $(2p^2)^1D$ resonance profile, which dominated the spectrum in Fig. 9*b*. The $(2s2p)^1P$ and $(2s2p)^3P$ state contributions have also signficantly reduced in intensity whilst the strength of the $(2s^2)^1S$ contribution has actually increased. Notice also the large increase in the asymmetry of the profiles for both $(2s^2)^1S$ and $(2p^2)^1P$ states and the large increase in the direct ionisation cross section.

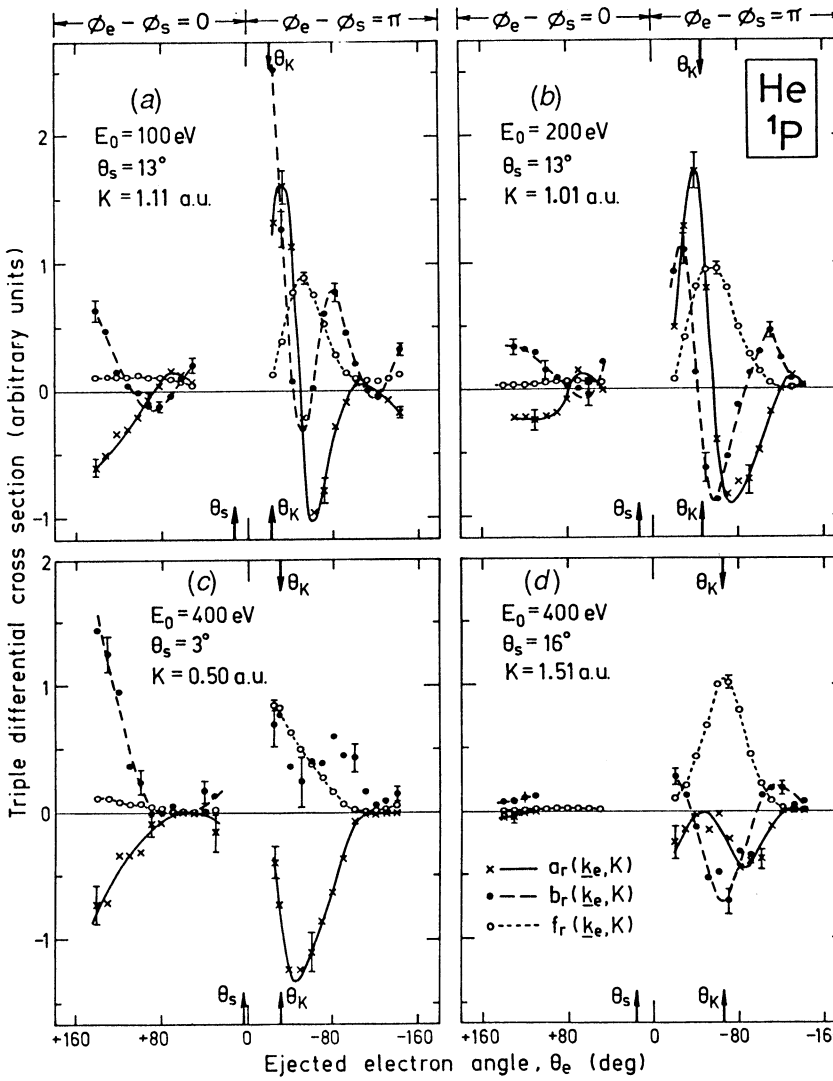

Fig. 11. The direct triple differential ionisation cross section f and resonance parameters $a_r(\mathbf{k}_e, \mathbf{K})$ and $b_r(\mathbf{k}_e, \mathbf{K})$ for the $(2s2p)^1P$ resonance in helium plotted as a function of the ejected electron angle θ_e for (*a*) incident electron energy E_0 of 100 eV and scattered electron angle $\theta_s = 13°$, (*b*) E_0 = 200 eV and $\theta_s = 13°$, (*c*) $E_0 = 400$ eV, $\theta_s = 3°$, and (*d*) $E_0 = 400$ eV, $\theta_s = 16°$ (Lower and Weigold 1990). The data are normalised by setting the maximum value of f under the ^1S resonance equal to unity. The momentum transfer directions θ_K are as shown.

Figs 10*a* and 10*b* show a sample of the results obtained for 200 eV incident electrons scattered through 13°. Fig. 10*a* illustrates dramatically in the case of the $(2p^2)^1D$ and $(2s2p)^1P$ states how the amplitudes for direct and resonant ionisation can interfere destructively, giving rise to localised reductions in the ionisation cross section due to the presence of additional reaction paths. The spectrum of Fig. 10*b* was collected in the recoil region $\phi_e = 0$, where scattered and ejected electrons are collected on the same side of the incident beam. In this region, for the present kinematical conditions, the direct ionisation cross section is always small and the resonance profiles are usually quite symmetric ($b_r \gg a_r$). The $(2s2p)^3P$ profile is no longer evident in either spectra at 200 eV, in contrast to the 100 eV spectra (Figs 9*a* and 9*b*). This is because the excitation of this state is optically forbidden and can only be achieved through the exchange of incident and target electrons, the probability of excitation through this process decreasing rapidly with increasing incident energy.

Values for a_r, b_r and f_r deduced from the fitting of individual ejected electron spectra for the $(2s^2)^1S$, $(2s2p)^1P$ and $(2p^2)^1D$ resonances show rapid variations as a function of θ_e. Fig. 11 shows the results for the $(2s2p)^1P$ state for four different combinations of incident energies and scattering angles. Since absolute cross sections were not obtained the results have been normalised to the maximum value of the direct ionisation cross section under the $(2s^2)^1S$ resonance profile at each particular energy and scattering angle, and this maximum has been arbitrarily set to 1 unit in the figure.

The direct ionisation cross section f for each incident energy and scattered electron angle appears in essentially two lobes. The major lobe occurs approximately in the momentum transfer direction and may be associated with binary encounters between incident and target electrons. The second occurs roughly 180° away and can be associated with recoil collisions involving momentum transfer to the residual ion.

In the binary region ($\phi_e = \pi$), the direction at which the direct ionisation cross section maximises varies significantly with the different kinematical conditions employed in each experiment. For the 100 eV/13° measurement this maximum occurs at approximately 52°, for the 200 eV/13° measurement at 56°, and for the 400 eV/16° at 66°. These angles respectively represent displacements of 31°, 10° and 0° from the direction of momentum transfer **K**. For the 400 eV/3° measurements the binary peak is only partially mapped out due to mechanical restrictions in the apparatus and hence the exact angle at which it maximises is not clear. The available data does, however, indicate a maximum near the direction of momentum transfer. The increasing proximity, with increasing incident energy, of the direction of momentum transfer with the direction at which the direct ionisation cross section maximises, can be easily understood in the context of the first Born approximation, in which the momentum transfer direction is the symmetry axis for the direct ionisation process. In the binary direction the cross section is determined by the target electron momentum distribution (McCarthy and Weigold 1976). The He $(1s)^2$ momentum distribution peaks at zero recoil momentum, i.e. along the momentum transfer direction, which is the direction of minimum recoil momentum (equation 2).

In the so-called recoil region (where $\mathbf{k}_e$ is in the $-\mathbf{K}$ direction) the strength of the direct ionisation process is generally much weaker than in the binary collision region for the kinematical conditions presently employed. This effect is most marked in the high momentum transfer 400 eV/16° measurement.

From equations (15) and (16), it is seen that the resonance parameters $a_r(\mathbf{k}_e,\mathbf{K})$ and $b_r(\mathbf{k}_e,\mathbf{K})$ for each resonance r are determined by complicated combinations of interfering amplitudes from the competing processes of direct and resonant ionisation. For this reason it is difficult to give a physical interpretation to their angular behaviour, or to explain observed differences between the results obtained under different kinematical conditions. In the absence of a direct contribution (i.e. for $I_\mu = 0$) $a_r = 0$ and the b_r depend only on the J_μ and $V_{\bar{E}_\mu}$ (equations 15 and 17), where J_μ expresses the probability of transfer of momentum to the atomic target and $V_{\bar{E}_\mu}$ the subsequent decay into the continuum. Thus for the ^{1}P resonance decaying to the ^{2}S ground state helium ion, only $l = 1$ partial waves are involved and b should vary as cos θ. Fig. 11 immediately shows that it is the direct ionisation matrix elements I_μ which have the dominant influence on the resonance cross section. The figure also shows that $a_r \to 0$ as $f_r \to 0$ as required by expressions (15) and (17).

For each resonance and at each energy and scattering angle, the a_r and b_r parameters both show smooth oscillation between positive and negative values as the ejection angle varies. Positive values of b_r correspond to constructive interference between direct and resonant ionisation amplitudes, resulting in localised increases in the triple differential ionisation cross section. Negative values of b_r are related to a decrease in the cross section due to the effects of destructive interference. Positive values of a_r correspond to a profile showing a minimum followed by a maximum in the sense of increasing ejection energy, whilst the reverse occurs when a_r is negative.

A strong correlation between the oscillatory behaviour of both resonance parameters is evident from the figure. Similar results are obtained for the ^{1}S and ^{1}D resonances (Lower and Weigold 1990). In the binary collision region ($\phi_s = 0$, $\phi_e = \pi$), the amplitude of oscillation in both a_r and b_r generally peaks in the neighbourhood of the momentum transfer direction and the direction for the maximum of the direct cross section f. In the recoil region, the values of a_r and b_r are in general very much smaller than in the binary region, as is the direct cross section. Excepted are the results from the 400 eV/3° measurement in which the behaviour of both parameters differs substantially from the other cases.

The results for all three resonances show strong interference, both constructive and destructive, between the direct and resonance amplitudes. The resonance parameters show even more rapid variation in magnitude as a function of the ejected electron angles than does the direct cross section. Although the peak structures in a_r and b_r are correlated with the direction of the momentum transfer θ_K, as is that for the direct cross section f_r, the correlation is not simple. Considerable amount of theoretical effort is needed to explain the data. First order theories, such as the plane wave Born approximation, are inadequate since they would give the $\mathbf{K}$ direction as a symmetry axis, which is clearly in violation of the measurements. The data depend sensitively on the phases between the direct and resonant ionisation amplitudes, and therefore provide sensitive tests for any theoretical model for the ionisation process.

5. Summary

Three separate recent (e,2e) measurements on atoms have been discussed. These measurements show the richness of information that can be obtained by application of this technique. Two of the measurements involve the determination of structure information using electron momentum spectroscopy. One is the first direct measurement of the momentum distribution of an electron in an excited atomic state, which has also been oriented by optical pumping with right-hand circularly polarised light. This study opens up exciting prospects for investigating the detailed structure of transient and excited species of atoms and molecules, and for observing momentum distributions from oriented and aligned molecules. The other case was a detailed study of argon. This study included the measurement of momentum profiles for orbitals occupied in the HF ground state as well as those for orbitals which are not occupied in the HF ground state but which play an important role in correlation effects. It allowed these initial state correlations to be identified and measured quantitatively. This was also true for final state correlations, which are especially important in the inner valence region. Quantitative measurements were made of the spectroscopic factors for transitions belonging to the different symmetry manifolds. These spectroscopic factors were found to be energy independent, as they must be if they are purely a function of the structure of the target and ion. When initial state correlations are negligible, the spectroscopic factors were also shown to be momentum independent. They were used to derive an unambiguous orbital energy, which is in excellent agreement with the HF orbital energy.

The final example was the application of the (e,2e) technique to investigate the interference between the direct and resonance ionisation amplitudes in the region of the $(2s^2)^1S$, $(2s2p)^3P$, $(2p^2)^1D$ and $(2s2p)^1P$ autoionising resonances in helium. The results show that there is very strong correlation between the direct and resonance amplitudes.

Acknowledgment

I am grateful to the Australian Research Council for support of this work.

References

Amusia, M., and Kheifets, A. S. (1985). *J. Phys.* B **18**, L679.
Amusia, M., and Kheifets, A. S. (1990). personal communication.
Balashov, V. V., Lipovetskii, S. S., Pavilichenkov, A. V., Polyudov, A. N., and Senashenko, V. S. (1971). *Opt. Spectrosc.* **32**, 4.
Balashov, V. V., Lipovetskii, S. S., and Senashenko, V. S. (1972). *Zh. Eksp. Teor. Fiz.* **63**, 1622.
Dyall, K. G. (1980). Ph.D. Thesis, Monash University.
Hibbert, A., and Hansen, J. E. (1987). *J. Phys.* B **20**, L245.
Lower, J., and Weigold, E. (1990). *J. Phys.* B (in press).
Lower, J., and Weigold, E. (1989). *J. Phys.* E **22**, 421.
McCarthy, I. E., Pascual, R., Storer, P., and Weigold, E. (1989). *Phys. Rev.* A **40**, 3041.
McCarthy, I. E., and Weigold, E. (1976). *Phys. Rep.* **27C**, 275.
McCarthy, I. E., and Weigold, E. (1988). *Rep. Prog. Phys.* **51**, 299.
Mitroy, J. D., Amos, K. A., and Morrison, I. (1984). *J. Phys.* B **17**, 1659.
Shore, B. W. (1967). *J. Opt. Soc. Am.* **57**, 881.
Tweed, R. J. (1976). *J. Phys.* B **9**, 1725.
von Niessen, W. (1987). personal communication.

Weigold, E., Hood, S. T., and Teubner, P. J. O. (1973) *Phys. Rev. Lett.* **30**, 475.
Weigold, E., and Zheng, Y. (1990). In preparation.
Zheng, Y. (1989). Ph.D. Thesis, Flinders University.
Zheng, Y., McCarthy, I. E., Weigold, E., and Zhang, D. (1990). *Phys. Rev. Lett.* **64**, 1358.

Manuscript received 7 May, accepted 28 May 1990